A. Romero-Calvo, F. Garrone, A.J. Garcia-Salcedo, I. Rivoalen, G. Cano-Gomez, E. Castro-Hernandez, F. Maggi
Free Surface Reconstruction of Opaque Liquids in Microgravity. Part 2: Drop Tower Campaign
Acta Astronautica, Vol. 189, 2021, p. 269-277
doi:10.1016/j.actaastro.2021.07.020

Free surface reconstruction of opaque liquids in microgravity. Part 2: drop tower campaign

Á. Romero-Calvo[a,b,*], F. Garrone[b], A. J. García-Salcedo[b], I. Rivoalen[b], G. Cano-Gómez[c], E. Castro-Hernández[d] and F. Maggi[b]

[a]Department of Aerospace Engineering Sciences, University of Colorado Boulder, CO, United States
[b]Space Propulsion Laboratory, Department of Aerospace Science and Technology, Politecnico di Milano, Via Giuseppe La Masa, 34, 20156, Milan, Italy
[c]Departamento de Física Aplicada III, Universidad de Sevilla, Avenida de los Descubrimientos s/n, 41092, Sevilla, Spain
[d]Departamento de Ingeniería Aeroespacial y Mecánica de Fluidos, Universidad de Sevilla, Avenida de los Descubrimientos s/n, 41092, Sevilla, Spain

ARTICLE INFO

Keywords:
Liquid interface
3D reconstruction
Microgravity
Ferrofluids
Magnetic liquid sloshing

ABSTRACT

This paper addresses the operation in microgravity of a surface reconstruction device whose design is detailed in the first part of the manuscript. The system, employed during the drop tower campaign of the UNOOSA DropTES 2019 StELIUM experiment, studies the axisymmetric and lateral oscillations of a ferrofluid solution in microgravity. The free liquid surface is reconstructed in a cylindrical tank and relevant metrics of the magnetic sloshing problem, such as contact angles, hysteresis parameters, natural oscillation frequencies, or damping ratios, are derived. The result is a rich and unique database where several phenomena of scientific and technological interest are reported for the first time. The dependence of the fundamental axisymmetric and lateral modal frequencies with the applied magnetic field is consistent with the literature and past experiments. Although the detection system was designed and built using low-cost hardware, high-quality results are obtained.

1. Introduction

The forced movement of liquids in partially filled tanks is commonly known as liquid sloshing [1]. The understanding of this phenomenon is of major importance for the study and characterization of the dynamics of space vehicles [2, 3]. As a way to control the position of liquids in low-gravity environments, the application of electric [4] and magnetic [5–10] fields has been proposed to generate a gravity-equivalent restoring force. The magnetic approach receives the name of *Magnetic Positive Positioning (MP^2)*.

The characterization of the natural oscillation frequencies of magnetic liquids is a first and fundamental step towards the development of MP^2 technologies, such as Tuned Magnetic Liquid Dampers [11, 12] or passive and active positioning devices [10]. The need for accurate simulation frameworks has motivated the development of coupled quasi-analytic [13] and numerical models [14], as well as the execution of microgravity experiments [15, 16]. As part of these efforts, the UNOOSA DropTES 2019 StELIUM (Sloshing of magnEtic LIqUids in Microgravity) experiment studied the free surface oscillations of a ferrofluid solution when subjected to an inhomogeneous magnetic field in microgravity [17]. The experiment was launched in November 2019 at ZARM's drop tower, completing a total of four catapult drops.

The accurate measurement and characterization of the oscillatory magnetic liquid dynamics is one of the major technical challenges of StELIUM. Several different technologies have been historically employed to accomplish this task. Among them, displacement sensors [11, 18–21], dynamometers [22], lateral cameras [7, 9, 23–27] or ultrasonic Doppler shift devices [19, 28, 29]. In the last decades, the increase in computational power has motivated the application of optical methods, such as stereo imaging [30], digital image correlation [31–35], pattern fringe reflectometry [36, 37], or particle image velocimetry [38, 39]. Alternative approaches employ the movement of a float [40], or the distortion of a laser on the surface [41] to obtain liquid level measurements. These approaches are hardly applicable to the StELIUM experiment, whose design is highly conditioned by the opaque nature of ferrofluids and the overwhelming role of surface tension in low-gravity environments. Besides, drop tower experiment setups must be compact, autonomous, highly resistant to impacts, and reliable. These conditions motivate the development of a new surface reconstruction system.

In the first part of this paper [42], a novel surface reconstruction approach is described and tested on ground. The system correlates the observations of a projected laser pattern with the height of an opaque fluid surface. The resulting Sloshing Detection Subsystem (SDS) of StELIUM is an inexpensive, non-invasive and highly adaptable device designed to (i) reconstruct the free surface of the magnetic liquid, (ii) study the first two sloshing frequencies and modal shapes of the oscillation, and (iii) compute their corresponding damping ratios.

This paper describes the operation of the SDS in microgravity, and presents the results of the experimental campaign at ZARM's drop tower. An overall description of the setup is first given in Sec. 2, followed by further details on the line-laser-based operation in Sec. 3. Microgravity results are presented in Sec. 4 and conclusions are finally given in Sec. 5.

*alvaro.romerocalvo@colorado.edu
ORCID(s): 0000-0003-3369-8460 (Á. Romero-Calvo)

2. The StELIUM experiment

The StELIUM project studies the axisymmetric and lateral sloshing of magnetic liquids in microgravity [17]. The experiment was launched four times at ZARM's drop tower in the framework of the UNOOSA DropTES 2019 campaign. During each drop, which provides 9.3 second of microgravity conditions, a ferrofluid solution is exposed to a static, inhomogeneous magnetic field and a lateral sinusoidal displacement is applied to trigger the lateral sloshing waves. The strength of the magnetic field, which is proportional to the coils current intensity (I), and the angular velocity of the excitation (ω_e), are changed between drops as described in Tab. 1.

From a systems engineering perspective, the experiment setup of StELIUM is subdivided into actuation, structural, magnetic, and detection subsystems. This setup, represented in Fig. 1, is distributed among two identical assemblies that include a partially filled Plexiglas tank surrounded by a coil. Both components stand upon a platform bolted to a linear slider. A stepper engine actuates both sliders simultaneously and imposes a lateral excitation in the middle of the drop. The SDSs are located at the top of each vessel to measure the dynamic response of the free ferrofluid surface. Further details can be consulted in Ref. 17.

Figure 1: Drop tower capsule of StELIUM after integration at ZARM's drop tower [17].

Table 1
StELIUM test matrix. Each drop is configured based on the excitation frequency ω_e and the coils current intensity I.

Drop	ω_e (rad/s)	I(A)
1	6.5	20
2	3.3	10
3	3.3	0
4	5	15

2.1. Sloshing Detection Subsystem (SDS)

The need for an inexpensive, non-invasive, highly adaptable, and reliable surface reconstruction system motivates the design of the SDS in the first part of this paper [42]. Its operation is based on the projection of a laser pattern over the opaque ferrofluid surface and the triangulation of such pattern with camera measurements.

The basic components of the SDS are twenty laser pointers, one line laser and a GoPro Hero 5 Session camera that records their projection in the retinal frame. In order to ease the detection of higher order oscillations, the laser pointers form three concentric circular rings with radii corresponding to the theoretical peaks of the first three lateral sloshing modes in microgravity. The line laser projects a straight line that crosses the center of the vessel, and its deformation unveils the shape of the interface. This continuous measurement was used in the final configuration of the SDS. The GoPro Hero 5 Session camera is placed at the center of the structure and works at 4K resolution and 30 fps frame rate. The resulting video measurements are processed by adopting the theoretical framework described in Ref. 42.

Laser observations are complemented by a VL53L0X time-of-flight sensor that measures the mean ferrofluid height in a region covering approximately half of the free surface. This value is used to provide redundant estimations of the oscillation frequencies. Besides, a Photron Fastcam MC-2 obtains lateral images of the free surface wave. The GoPro and Photron cameras are synchronized with the blink of a LED at the beginning of each drop.

A fast and low-cost development is achieved by selecting commercial off-the-shelf Arduino electronics. The electronic components are mounted in the 3D printed PLA structure depicted in Fig. 2, that provides high structural resistance with a low mass penalty. These are key characteristics for withstanding the 50 g deceleration load of ZARM's drop tower. The subsystem is powered by a 5V USB cable, and is interfaced with the Capsule Control System by means of a single trigger line.

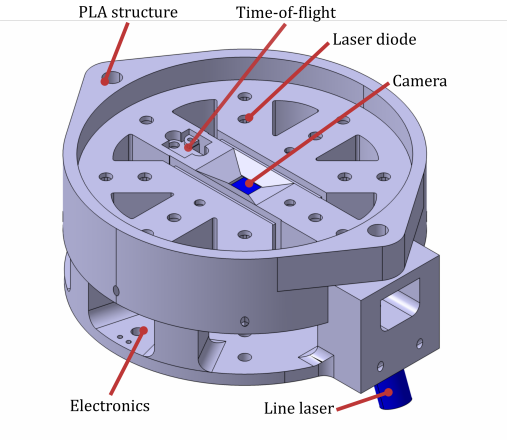

Figure 2: Bottom view of the Sloshing Detection Subsystem.

2.2. ZARM's drop tower campaign

The integrated experiment setup, depicted in Fig. 1, was extensively tested before the first drop. It was observed that the actuation mechanism did not induce oscillations in the direction perpendicular to the excitation. However, the original configuration of the SDS (with 20 vertical laser pointers covering the whole surface) gives rise to several laser reflections, as already noted in the first part of the paper [42].

Unlike the vertical laser pointers, the laser line is tilted approximately 20°. This leads to larger deformations of the projected line, enhanced resolutions, and elimination of laser reflections, as none of the reflected lines crosses the lens of the camera. Since orthogonal modes were expected to be negligible and had little scientific interest, it was decided to disconnect the laser pointers and rotate the SDS 90°. As a counterpart, the Time-of-Flight sensor was displaced from the peak of the lateral wave, reducing its effectivity. Two laser diodes perpendicular to the line were switched on to monitor the orthogonal sloshing modes, resulting in the laser pattern depicted in Fig. 3.

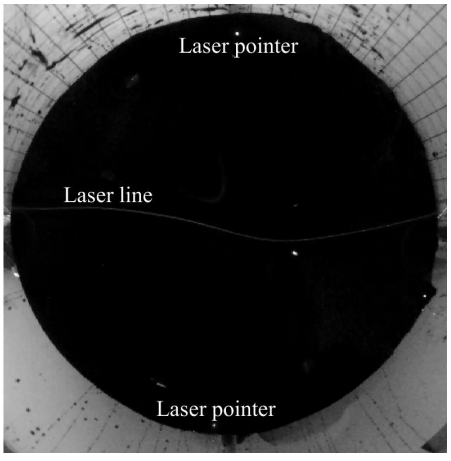

Figure 3: Laser pattern configuration.

3. Line laser system

3.1. Extraction algorithm

The position of the laser line is extracted in the retinal reference system for every video frame. This operation is based on the identification of the brightest pixels in the image, but is complicated by the sudden appearance of reflections at the surface. As with the laser-point-based operation [42], the definition and application of filters is key to ensure the robustness of the laser line reconstruction algorithm.

For each video frame, the line is computed by enforcing its continuity with respect to time and space. While space continuity is imposed by defining a maximum y-displacement between two contiguous pixels in the same time frame, the time continuity is applied by evaluating the y-displacement of each laser point between different time frames. In this regard, only small line displacements are expected between two consecutive time frames i and $i+1$. A time backward detection algorithm that derives the line in the frame i from values computed in the frame $i+1$ is implemented. The time backward approach improves the performance with a smoother time variation. Therefore, a Gaussian filter with standard deviation $\sigma_{\text{time}} = 25$ px centered on the line at the time frame $i+1$ is used to identify the brightest pixels at step i. The space continuity constriction is imposed by a Gaussian filter with $\sigma_{\text{space}} = 8$ px. Starting from the center of the line, the algorithm maps it in both the directions, ensuring a continuous reconstruction.

The manifestation of bright reflection points causes unwanted deviations in the reconstructed line. For this reason, an additional threshold in pixel brightness is imposed. Although in some cases the reflection cannot be removed, only minor perturbations have been observed in the results. Such perturbations are quickly corrected in consecutive time steps.

3.2. Reconstruction

The surface reconstruction algorithm developed in the first part of the paper [42] is applied to each point of the laser line to obtain its $\{X, Y, Z\}$ world coordinates. Although the original design assumes that the position and orientation of the camera with respect to the world reference system are known (i.e. trivial extrinsics transformation), the SDS assembly actually induces a slight tilting in the observer. The associated rotation matrix is estimated by means of Davenport's q algorithm [43] with measurements of the free surface contour taken instants before the catapult drop takes place. With this approach, it is assumed that the position of the camera and the ferrofluid surface are known in normal-gravity conditions. Small errors in the axial rotation of the camera-laser assembly are corrected by imposing a balanced meniscus profile in microgravity.

3.3. Processing

Different results of interest are obtained from the reconstructed laser line. Since the liquid is not able to settle before the end of the flight, the meniscus profile, which is a result of fundamental interest for the study and characterization of

the system, is computed by averaging the last (and weakest) lateral sloshing wave ($t > 8.5$ s) in world coordinates and fitting a function of the form

$$F(R) = a_0 + \sum_{i=1}^{5} a_i R^{2i}, \tag{1}$$

where $F(R)$ is the height of the meniscus with respect to the bottom of the tank, $R = \sqrt{X^2 + Y^2}$ is the radius, and $b_i \geq 0$ for numerical robustness. The apparent static contact angle between the meniscus and the wall is computed as

$$\theta_c = \frac{\pi}{2} - \arctan \frac{dF}{dR}\Big|_C, \tag{2}$$

with the radial derivative being taken at the contact line C.

The fundamental frequency can be directly obtained from the Fast Fourier Transform (FFT) of the displacement of the laser line in the retinal frame. Although this approach avoids the surface reconstruction step, it generally fails to reflect faster high-order frequencies and their associated damping ratios. Instead, the world coordinates of the laser line $\{\boldsymbol{X}(t), \boldsymbol{Y}(t), \boldsymbol{Z}(t)\}$ are projected in an appropriate modal base. For each time step, the overdetermined system

$$\boldsymbol{Z} - \boldsymbol{F}(\boldsymbol{X}, \boldsymbol{Y}) = \mathrm{M}(\boldsymbol{X}, \boldsymbol{Y})\boldsymbol{\eta}, \tag{3}$$

is solved with a least-squares algorithm, where $\mathrm{M}(\boldsymbol{X}, \boldsymbol{Y})$ is the matrix of axisymmetric and lateral modal shapes (i.e. each column contains the Z coordinates of a certain mode), and $\boldsymbol{\eta}$ is the vector of modal coefficients. It should be noted that $F(\boldsymbol{X}, \boldsymbol{Y})$ and $\mathrm{M}(\boldsymbol{X}, \boldsymbol{Y})$ are evaluated at the laser line. In this way, the influence of each mode is uniquely determined by its corresponding η coefficient.

The modal shapes $\mathrm{M}(\boldsymbol{X}, \boldsymbol{Y})$ are computed with the quasi-analytical model described in Ref. 13 assuming the non-magnetic case and the optimum contact angle hysteresis parameter Γ. Although the magnetic field has little influence in the modal shapes, the same cannot be said regarding the hysteresis parameter. The *free-edge condition* is characterized by $\Gamma = 0$, while the *stuck-edge condition* is associated with $\Gamma \to \infty$. In the StELIUM experiment, Γ adopts an intermediate value, and the modal shapes are qualitatively similar to those depicted in Fig. 4 for $\Gamma = 9.8$. The optimum Γ is estimated as the value that minimizes the total residual of the modal projection.

Finally, the FFT of each modal coefficient η is used to obtain the associated frequency after increasing the FFT resolution with zero-padding. The damping ratios are computed by means of the half-power bandwidth method as

$$\xi_n = \frac{1}{2}\frac{\Delta\omega_{-3dB}}{\omega_n}, \tag{4}$$

with ω_n being the natural frequency of mode n and $\Delta\omega_{-3dB}$ the frequency width between the -3 dB points surrounding ω_n. It should be noted that the robustness of this modal frequency estimation is dependent on the adequacy of the modal shapes employed in the analysis.

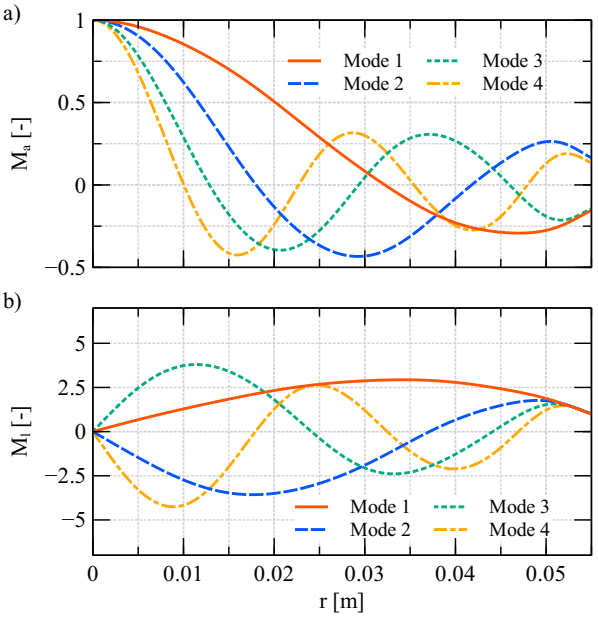

Figure 4: Theoretical, non-magnetic, a) axisymmetric and b) lateral modal shapes for $\Gamma = 9.8$ as a function of the radius [13].

4. Preliminary microgravity results

Orthogonal oscillations have a minimal incidence in the free surface evolution, which motivates the tilting of 90° of the SDS. Figure 5 shows the centered differential displacement between upper and lower laser control points in world

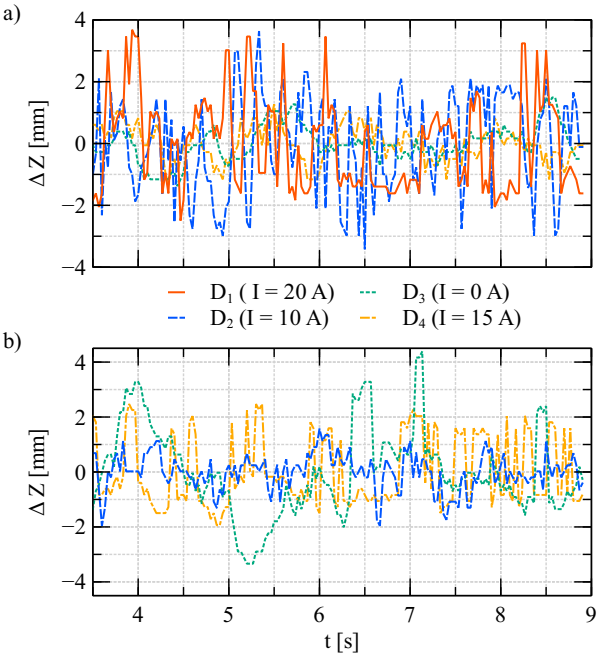

Figure 5: Centered differential displacement between upper and lower laser control points after the application of the lateral oscillation for a) top, and b) bottom containers in world coordinates.

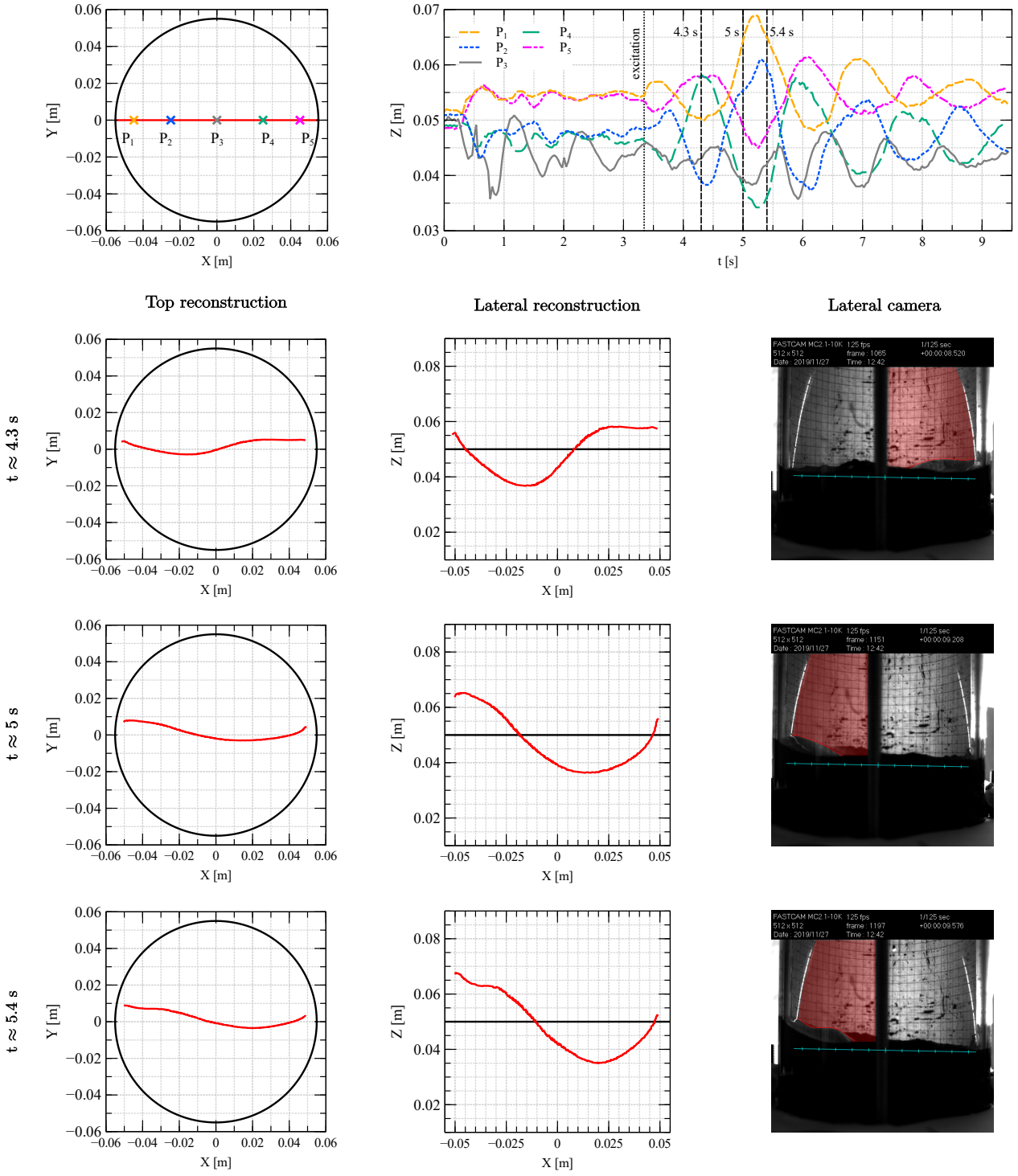

Figure 6: Surface line laser evolution of the top container during the second drop. On the top, the evolution in time of different surface points is depicted. The first and second columns represents the top and lateral reconstructions of the ferrofluid surface. On the third column, synchronized lateral images are shown.

coordinates for each experiment. This metric should reproduce a clear oscillatory evolution in the presence of orthogonal modes. However, such oscillatory behavior is generally not observed. Besides, the movement is characterized by a maximum amplitude of approximately ±3 mm after the lateral percussion is applied at $t \approx 3.5$ s, which is significantly smaller than the ±15 mm amplitude that characterizes the vertical displacement of the laser line. The small incidence

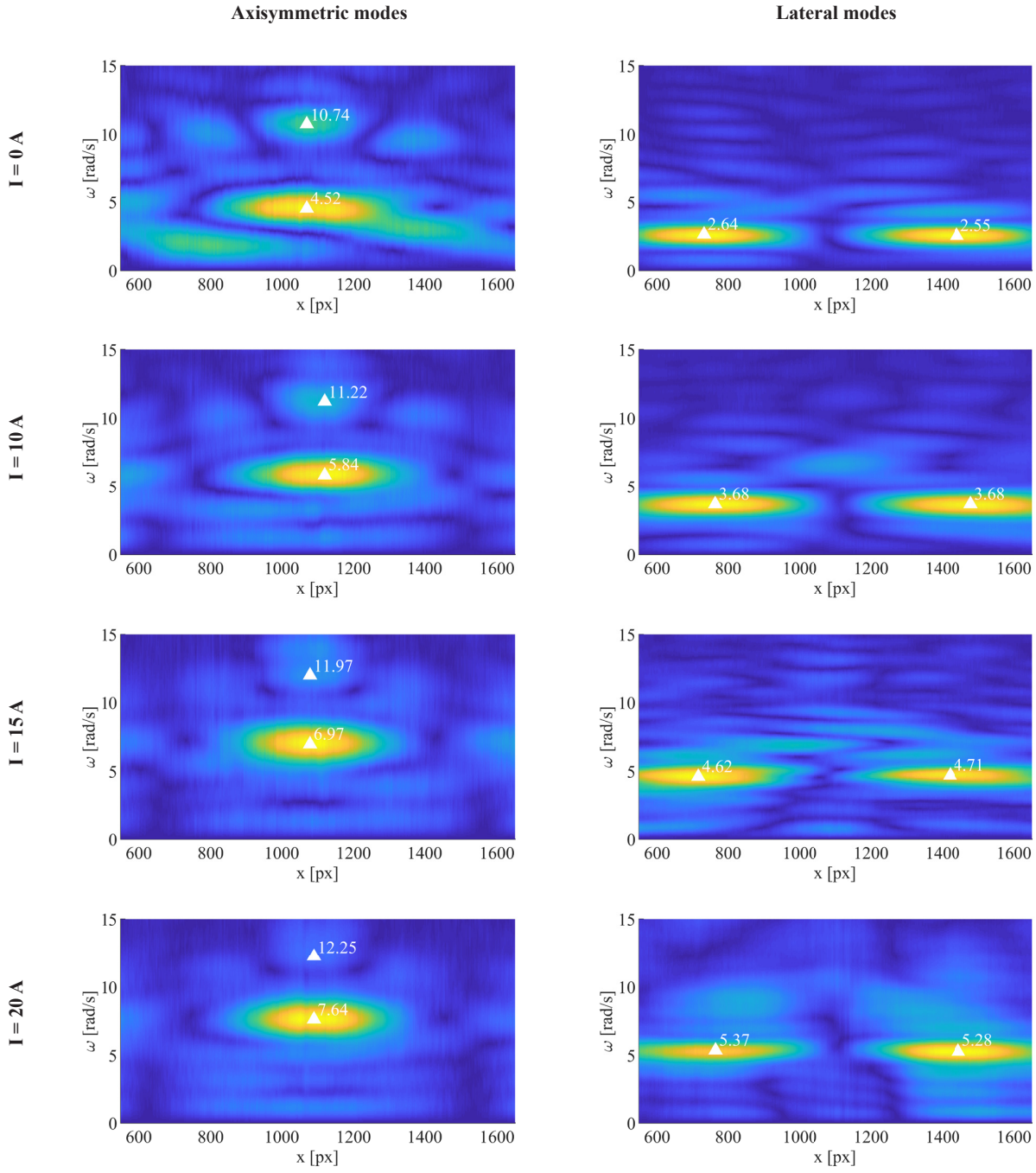

Figure 7: Fast Fourier Transform of the laser line for axisymmetric and lateral oscillations of the upper container.

of orthogonal modes in microgravity is then verified.

The position of the laser line is extracted and reconstructed as described in Sec. 3. The time evolution of five equally distributed points along the laser line is depicted in Fig. 6 for the top container and the second drop. After the start of the catapult drop, the flat surface evolves towards the characteristic curved meniscus. The central point experiences large oscillations while the radially distributed points remain practically unaltered. In other words, axisymmetric free surface oscillations are induced to the fluid after entering microgravity conditions. The imposition of a sinusoidal lateral displacement at $t \approx 3.5$ s [17] excites both axisymmetric and lateral modes, with the latter being clearly dominant over the former. In order to validate the output of the SDS, subsequent plots compare the projection of the laser line in the X-Z plane with lateral observations of the free surface at

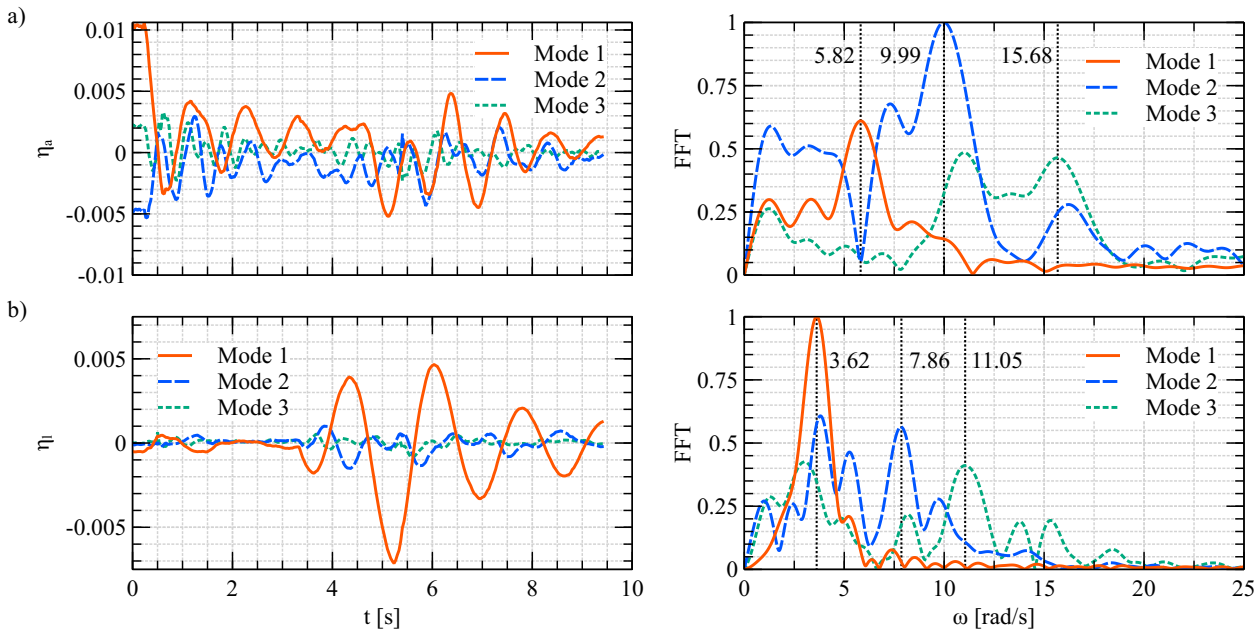

Figure 8: Axisymmetric (a) and lateral (b) modal projection coefficients (left) and their FFT (right) for the upper container and second drop ($I = 10$ A).

specific times. Although the convex meniscus hides part of the line, the peaks of the sloshing wave are still observable. Both measurements are in excellent agreement, validating the output of the SDS.

As detailed in Sec. 3.3, the fundamental free surface oscillation frequencies can be easily obtained by analyzing the movement of the laser line in the retinal frame. Figure 7 shows the axisymmetric and lateral FFT maps for the upper container. Each point in the x axis corresponds to a point of the laser line in the retinal frame. The FFT spectrum is expanded in the y (frequency) axis. The axisymmetric and lateral maps are computed in the time intervals $0-3.5$ s and $3.5-9.3$ s, respectively, to avoid cross-contamination, and the peaks are determined using a 2D peak locator[1]. While the fundamental axisymmetric frequency peak occupies the center of the line, the fundamental lateral frequency peak is displaced towards the contour. The latter is reached at an intermediate radius, reflecting that the hysteresis parameter Γ is neither 0 (free edge) nor ∞ (stuck edge) for lateral modes. The second axisymmetric mode is depicted as a higher-frequency peak in the center of the container. Due to the shape of the second mode, represented in Fig. 4, two symmetric peaks appear at $x = 800$ px and $x = 1400$ px. The second and third maxima of the fundamental and second axisymmetric modes, respectively, are reached at the contour, which is a typical characteristic of the free edge condition [16]. In other words, the hysteresis parameter Γ is approximately 0 for axisymmetric modes, and adopts an intermediate value for lateral modes. Higher-order modes, which experience a faster decay, are hardly observable with this approach.

[1] https://www.mathworks.com/matlabcentral/fileexchange/37388-fast-2d-peak-finder. Consulted: 24/09/2020

In order to improve the estimation of the modal frequencies, the modal projections are computed and analyzed as described in Sec. 3.3. Figure 8 shows the axisymmetric (top) and lateral (bottom) modal coefficients (left) and their FFT (right) for the upper container and second drop. As with Fig. 6, while the axisymmetric modes are triggered by both the catapult acceleration and the lateral excitation, only the latter induces a lateral oscillation. It is important to note that the experimental eigenmodes may differ from their theoretical estimations, causing some dependency between modal coefficients (i.e. their frequency spectrum will be *contaminated* by different modes). To minimize this effect, the FFT is computed in the 0-3.5 s time interval for the axisymmetric case, and between 3.5 and 9.3 s for the lateral case. Although the actual frequency peaks associated to those modes are clearly visible, the contamination effect is still present (i.e. the influence of the fundamental lateral mode on the spectrum of higher-order modes is manifested as spurious peaks with the same frequency).

The reconstructed laser line is analyzed as described in Sec. 3.3 for each experiment, resulting in an estimation of the contact angle θ_c, lateral hysteresis parameter Γ, first three axisymmetric and lateral natural frequencies $\omega_{a/l,i}$, and their corresponding damping ratios $\xi_{a/l,i}$. Results are summarized in Tab. 2 for upper and lower containers as a function of current intensity. The apparent contact angle associated to the upper container (Mean $M = 62.15°$, Standard Deviation $SD = 2.60°$) is significantly larger than for the lower container ($M = 52.91°$, $SD = 5.32°$), as determined by a two-sample t-test $t(5) = 3.07$ with p-value $p = 0.03$. The angle seems to increase with current intensity, but there is not a significant linear correlation between those variables (upper: correlation coefficient $r(2) = 0.79$, $p = 0.21$; lower:

Table 2
Experimental results from the modal projection approach described in Sec. 3.3 for contact angle, fundamental and second oscillation frequencies and damping ratios for axisymmetric and lateral waves, and lateral hysteresis parameter. The $I = 20$ A case for the lower container is estimated from time-of-flight sensor data.

	I [A]	θ_c [deg]	Γ [-]	$\omega_{a,1}$ [rad/s]	$\xi_{a,1}$ [-]	$\omega_{a,2}$ [rad/s]	$\xi_{a,2}$ [-]	$\omega_{a,3}$ [rad/s]	$\xi_{a,3}$ [-]	$\omega_{l,1}$ [rad/s]	$\xi_{l,1}$ [-]	$\omega_{l,2}$ [rad/s]	$\xi_{l,2}$ [-]	$\omega_{l,3}$ [rad/s]	$\xi_{l,3}$ [-]
Upper	0	60.52	16.75	4.52	0.19	9.99	0.10	14.34	0.07	2.58	0.21	7.22	0.06	11.61	0.04
	10	59.87	7.23	5.82	0.15	9.99	0.11	15.68	0.08	3.62	0.16	7.86	0.07	11.05	0.07
	15	62.36	7.11	7.05	0.14	10.91	0.13	16.46	N/A	4.60	0.12	7.965	N/A	13.99	0.08
	20	65.67	4.41	7.60	0.13	11.03	N/A	16.08	N/A	5.30	0.11	8.88	0.13	13.20	0.10
Lower	0	47.52	15.27	3.62	0.23	7.31	0.18	14.04	0.07	2.21	0.22	4.69	0.11	10.69	N/A
	10	53.07	4.88	5.41	0.16	9.33	0.12	13.95	N/A	3.36	0.17	9.01	0.06	14.02	0.03
	15	58.15	5.44	5.98	0.17	9.27	0.18	13.80	0.20	4.18	0.15	7.60	0.10	13.85	0.09
	20	-	-	-	-	-	-	-	-	*4.90*	-	*9.99*	-	*13.67*	-

$r(1) = 0.99$, $p = 0.10$). However, previous experiments with ferrofluid droplets report a dependence between contact angle and applied magnetic field [44–46]. Larger datasets are consequently required to prove statistical correlation. The hysteresis parameter Γ, that determines the shape of the lateral modes, is significantly larger for the non-magnetic case, and seems to decrease with the magnetic field. From a physical perspective, the magnetic field shifts the interface behavior from a stuck-edge to a free-edge condition. This may be associated with the increase of the magnetic Bond number, defined as the ratio between magnetic and surface tension forces [13], and the consequent shift from capillary (surface tension dominated) to inertial (magnetic force dominated) regimes. The magnetic Γ values are slightly larger for the upper container ($M = 6.25$, $SD = 1.59$) with respect to the lower container ($M = 5.16$, $SD = 0.40$), but this difference is not statistically significant ($t(3) = 0.90$, $p = 0.43$).

Table 2 also presents the three first modal oscillation frequencies for axisymmetric and lateral oscillations. In both cases, the fundamental sloshing frequency consistently increases with current intensity, while its corresponding damping ratio decreases. The fundamental frequencies are in excellent agreement with those reported in Fig. 7. However, the second axisymmetric frequency follows a more consistent positive trend with current intensity in Fig. 7 than in Tab. 2. As explained in Sec. 3.3, an imperfect matching between theoretical and experimental modal shapes is likely behind this behavior. Measurements from upper and lower containers are shifted approximately 0.8 rad/s (axisymmetric) and 0.3 rad/s (lateral) with respect to each other. Since the shift is constant with current intensity, it has to be produced by the non-magnetic parameters of the system, such as the contact angle. The well-defined dependence with current intensity is not repeated for higher-order modes, whose detection is complicated due to their faster decay and smaller prominence in the frequency spectrum. Again, this reflects the difficulties associated to the detection of faster waves. For the cells filled with "N/A", the frequency peak is so weak that the damping ratios cannot be computed.

The $I = 20$ A case is not fully reported in Tab. 2 for the lower container because of the unexpected disconnection of the laser line at the beginning of the catapult drop. However, as described in Sec. 2.1, a time-of-flight sensor is used to obtain redundant measurements of the lateral oscillation, a design choice that allows recovering useful information from this drop. Figure 9 shows the sensor data and its associated frequency spectrum. Since the sensor points towards the surface, the bending of the meniscus is perceived as a decrease in the laser range, which is also biased and distorted by the container cover and the highly reflective nature of the ferrofluid. Nevertheless, three peaks are clearly observed in the frequency spectrum, corresponding approximately to the

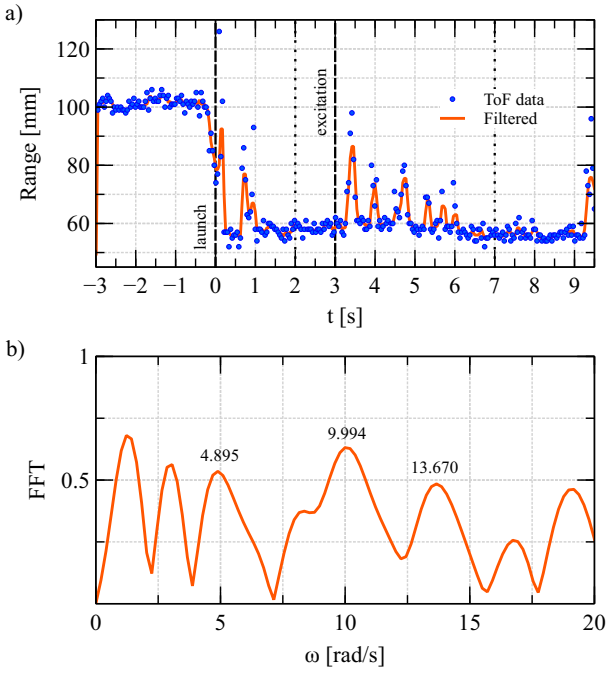

Figure 9: a) Laser time-of-flight measurements of the overall free surface position for the first drop ($I = 20$ A) and lower container, and b) FFT frequency spectrum computed between the dotted lines.

three first lateral modes.

The fundamental axisymmetric and lateral sloshing frequencies are represented in Fig. 10 and fitted with a function of the form

$$\omega(I) = b_0 I(1 - e^{-b_1 I}) + b_2, \tag{5}$$

that satisfies the conditions of zero slope in the origin and linear evolution for high current intensities reported in Ref. 13. The degrees of freedom of the fitting for the axisymmetric frequency of the lower container have been reduced by setting $p_1 = 0.218$, which is the same value as for the upper container, due to the availability of only three data points. In other words, the transient behavior has been artificially imposed. Error bands are built by identifying the non-zero-padded FFT resolution with the $\pm 3\sigma$ Gaussian interval, resulting in a standard deviation of 0.17 and 0.31 rad/s for lateral and axisymmetric modes, respectively. The linear fits, determined by the magnetic interaction, are practically parallel for upper and lower containers. A clear vertical shift between containers is also observed. As reported in the discussion of Tab. 2, this is caused by the slight differences in the non-magnetic parameters of the system (θ_c and Γ). It should be noted how the time-of-flight measurement fits nicely in the linear trend of the lower container, validating its employment as a backup system. The rest of points, computed from the FFT of the modal projection coefficients, are also in agreement with the peaks reported in Fig. 7 for the upper container. The curves exhibit the same qualitative behavior as in Refs. 13 and 16, with the non-magnetic frequencies being in excellent agreement with estimations from a low-gravity sloshing model [47].

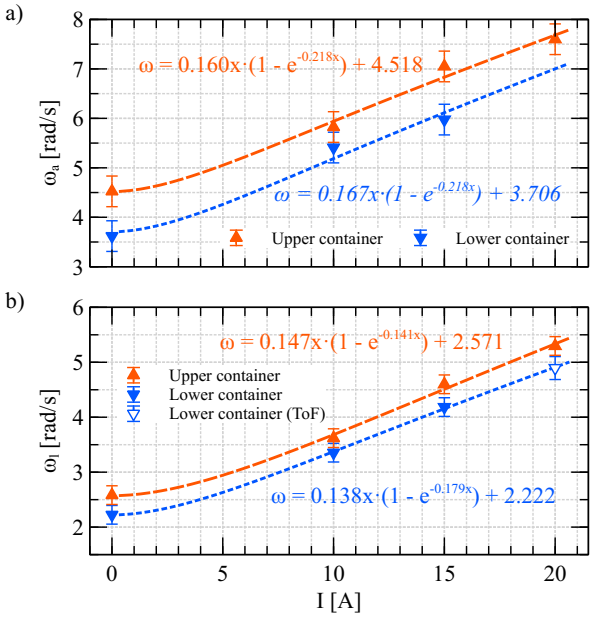

Figure 10: Fundamental a) axisymmetric and b) lateral free surface oscillation frequencies for upper and lower containers as a function of current intensity. A transient parameter $p_1 = 0.218$ is imposed in the fitting of the axisymmetric frequencies of the lower container. The error bands denote the standard deviation computed from the frequency resolution of the non-zero-padded FFT.

5. Conclusions

The Sloshing Detection Subsystem of StELIUM is an inexpensive, non-invasive, and highly adaptable device designed to reconstruct the shape of an opaque fluid surface and satisfy the technical and scientific requirements of this drop tower experiment. After introducing the theoretical foundations and assessing the on-ground performance of the system in the first part of the paper [42], this second part presents relevant scientific results obtained in microgravity conditions.

The application of a precise lateral impulse to the fluid results in a dominant lateral sloshing wave. This motivates the use of the line laser, instead of the less accurate vertical laser diodes, in the reconstruction of the free surface. Lateral images of the sloshing wave are compared with the measurements to validate the reconstructed line profile, which is successfully employed to obtain the fundamental sloshing frequency and apparent contact angles. Projections on an analytical modal set [13] serve to obtain the second and third oscillation frequencies and damping ratios as well as the lateral hysteresis parameter. However, the rapid decay of those modes undermines the efforts to extract a clear dependence with the inputs of the experiment. The complementary time-of-flight sensor, installed to obtain redundant measurements of the fundamental frequency, proves its utility by recovering useful data from a drop where the main system suffers a malfunction.

The results of the analysis unveil several phenomena of scientific and technical interest. Those include the growth of the apparent contact angle with the applied magnetic field, the unexpected increase of the hysteresis parameter in the non-magnetic scenario, or the evolution of modal frequencies and damping ratios with the current intensity applied to the coils. Future works should address these observations with appropriate analytical and numerical tools.

Competing Interests

The authors declare no competing interests.

Funding Sources

This work was supported by the United Nations Office for Outer Space Affairs (UNOOSA), the Center of Applied Space Technology and Microgravity (ZARM) and the German Space Agency (DLR) in the framework of the UNOOSA DropTES Programme 2019. Further financial and academic support was obtained from Ferrotec Corporation, Politecnico di Milano, the University of Seville, the European Space Agency (ESA) and the European Low Gravity Research Association (ELGRA).

Acknowledgements

The authors acknowledge the financial, technical and academic support offered by UNOOSA, DLR, ZARM, Ferrotec Corporation, Politecnico di Milano and the University of Seville. We also thank ESA and ELGRA for financing the presentation of this work at the 70th International Astronautical Congress (IAC) and the 26th ELGRA Biennial Symposium and General Assembly. This project is in debt with ZARM's drop tower engineers Jan Siemer and Fred Oetken, ZARM's point of contact Dr Thorben Könemann and UNOOSA's point of contact Ayami Kojima for their endless support. We finally would like to thank the technicians Giovanni Colombo, Alberto Verga and the PhD student Riccardo Bisin from the Space Propulsion Laboratory (SPLab) of Politecnico di Milano for their academic and technical assistance, as well as the rest of members of this research group for contributing to the creation of an extraordinary professional and human environment.

References

[1] W. C. Reynolds, H. M. Satterlee, The Dynamic Behavior of Liquids in Moving Containers, NASA SP-106, 1966.

[2] A. Myshkis, R. Wadhwa, Low-gravity fluid mechanics: mathematical theory of capillary phenomena, Springer, 1987.

[3] F. Dodge, The New Dynamic Behavior of Liquids in Moving Containers, Southwest Research Institute, San Antonio, TX, 2000.

[4] D. Chipchark, Development of expulsion and orientation systems for advanced liquid rocket propulsion systems, Tech. Rep. RTD-TDR-63-1048, Contract AF04 (611)-8200, USAF (1963).

[5] S. Papell, Low viscosity magnetic fluid obtained by the colloidal suspension of magnetic particles, US Patent 3215572 (1963).

[6] J. Marchetta, J. Hochstein, Fluid capture by a permanent ring magnet in reduced gravity, in: 37th Aerospace Sciences Meeting and Exhibit, 1999, aIAA Paper No. 1999-0845.

[7] J. Martin, J. Holt, Magnetically actuated propellant orientation experiment, controlling fluid motion with magnetic fields in a low-gravity environment, Tech. Rep. TM-2000-210129, M-975, NAS 1.15:210129, NASA (2000).

[8] J. Marchetta, J. Hochstein, Simulation and dimensionless modeling of magnetically induced reorientation, in: 38th Aerospace Sciences Meeting and Exhibit, 2000, aIAA Paper No. 2000-0700.

[9] J. G. Marchetta, A. P. Winter, Simulation of magnetic positive positioning for space based fluid management systems, Mathematical and Computer Modelling 51 (9) (2010) 1202 – 1212.

[10] A. Romero-Calvo, F. Maggi, H. Schaub, Prospects and challenges for magnetic propellant positioning in low-gravity, in: Proceedings of the AAS Guidance, Navigation and Control Conference, Breckenridge, Colorado, 2020, pp. 497–515.

[11] K. Ohno, M. Shimoda, T. Sawada, Optimal design of a tuned liquid damper using a magnetic fluid with one electromagnet, Journal of Physics: Condensed Matter 20 (20) (2008) 204146.

[12] K. Ohno, H. Suzuki, T. Sawada, Analysis of liquid sloshing of a tuned magnetic fluid damper for single and co-axial cylindrical containers, Journal of Magnetism and Magnetic Materials 323 (10) (2011) 1389–1393.

[13] A. Romero-Calvo, G. Cano Gómez, E. Castro-Hernández, F. Maggi, Free and Forced Oscillations of Magnetic Liquids Under Low-Gravity Conditions, Journal of Applied Mechanics 87 (2), 021010 (12 2020).

[14] A. Romero-Calvo, M. Herrada, G. Cano-Gómez, H. Schaub, Advanced numerical simulation of magnetic liquid sloshing in microgravity, in: Proceedings of the 71st International Astronautical Congress (IAC) - The CyberSpace Edition, 2020.

[15] A. Romero-Calvo, T. Hermans, G. Cano Gómez, L. Parrilla Benítez, M. Herrada Gutiérrez, E. Castro-Hernández, Ferrofluid dynamics in microgravity conditions, Proceedings of the 2nd Symposion on Space Educational Activities (2018).

[16] A. Romero-Calvo, M. A. Herrada, T. H. Hermans, L. P. Benítez, G. Cano-Gómez, E. Castro-Hernández, Axisymmetric ferrofluid oscillations in a cylindrical tank in microgravity, Microgravity Science and Technology, *under review* (2020).

[17] A. Romero-Calvo, A. García-Salcedo, F. Garrone, I. Rivoalen, G. Cano-Gómez, E. Castro-Hernández, M. H. Gutiérrez], F. Maggi, StELIUM: A student experiment to investigate the sloshing of magnetic liquids in microgravity, Acta Astronautica 173 (2020) 344 – 355.

[18] F. T. Dodge, L. R. Garza, Simulated low-gravity sloshing in spherical, ellipsoidal, and cylindrical tanks, Journal of Spacecraft and Rockets 7 (2) (1970) 204–206.

[19] T. Sawada, Y. Ohira, H. Houda, Sloshing motion of a magnetic fluid in a cylindrical container due to horizontal oscillation, Energy Conversion and Management 43 (3) (2002) 299–308.

[20] F. T. Dodge, L. R. Garza, Free-surface vibrations of a magnetic liquid, Journal of Engineering for Industry 94 (1) (1972) 103–108.

[21] T. Sawada, S. Shibata, Y. Matsubara, H. Kikura, T. Tanahashi, Liquid sloshing of a magnetic fluid in a rectangular container, Nihon Kikai Gakkai Ronbunshu, B Hen/Transactions of the Japan Society of Mechanical Engineers, Part B 60 (572) (1994) 1250–1255.

[22] F. T. Dodge, L. R. Garza, Experimental and Theoretical Studies of Liquid Sloshing at Simulated Low Gravity, Journal of Applied Mechanics 34 (3) (1967) 555–562.

[23] T. Coney, J. Salzman, Lateral sloshing in oblate spheroidal tanks under reduced- and normal-gravity conditions, Tech. Rep. TN D-6250, NASA (1971).

[24] S. Sudo, H. Hashimoto, A. Ikeda, K. Katagiri, Some studies of magnetic liquid sloshing, Journal of Magnetism and Magnetic Materials 65 (2) (1987) 219 – 222.

[25] N. Ramachandran, F. Leslie, P. Peters, R. Sisk, A novel method of gradient forming and fluid manipulation in reduced gravity environments, in: 36th AIAA Aerospace Sciences Meeting and Exhibit, 1998, AIAA Paper 1998-733.

[26] R. Zhou, M. Vergalla, S. Chintalapati, D. Kirk, H. Gutierrez, Experimental and numerical investigation of liquid slosh behavior using ground-based platforms, Journal of Spacecraft and Rockets 49 (6) (2012) 1194–1204.

[27] G. Lapilli, D. Kirk, H. Gutierrez, P. Schalhorn, B. Marsell, J. Roth, J. Moder, Results of microgravity fluid dynamics captured with the spheres-slosh experiment, in: Proceedings of the 66th International Astronautical Congress, Jerusalem, Israel, 2015.

[28] Y. Takeda, Velocity profile measurement by ultrasound doppler shift method, International Journal of Heat and Fluid Flow 7 (4) (1986) 313–318.

[29] T. Sawada, H. Kikura, T. Tanahashi, Kinematic characteristics of magnetic fluid sloshing in a rectangular container subject to non-uniform magnetic fields, Experiments in Fluids 26 (3) (1999) 215–221.

[30] Y. Qian, M. Gong, Y. Yang, Stereo-based 3d reconstruction of dynamic fluid surfaces by global optimization, in: 2017 IEEE Conference on Computer Vision and Pattern Recognition (CVPR), Honolulu, HI, USA, 2017.

[31] L. Chatellier, S. Jarny, F. Gibouin, L. David, A parametric piv/dic method for the measurement of free surface flows, Experiments in Fluids 54 (3) (2013) 1488.

[32] C. H. Chien, T. H. Su, C. J. Huang, Y. J. Chao, W. L. Yeh, P. S. Lam, Application of digital image correlation (dic) to sloshing liquids, Optics and Lasers in Engineering 115 (2019) 42 – 52.

[33] Y. Ding, F. Li, Y. Ji, J. Yu, Dynamic fluid surface acquisition using a camera array, in: 2011 International Conference on Computer Vision, Barcelona, Spain, 2011.

[34] J. Ye, Y. Ji, F. Li, J. Yu, Angular domain reconstruction of dynamic 3d fluid surfaces, in: 2012 IEEE Conference on Computer Vision and Pattern Recognition, Providence, RI, USA, 2012.

[35] S. Thapa, N. Li, J. Ye, Dynamic fluid surface reconstruction using

deep neural network, in: 2020 IEEE/CVF Conference on Computer Vision and Pattern Recognition (CVPR), 2020, pp. 21–30.

[36] H. Zhang, S. Han, S. Liu, S. Li, L. Ji, X. Zhang, 3D shape reconstruction of large specular surface, Appl. Opt. 51 (31) (2012) 7616–7625.

[37] L. Huang, C. S. Ng, A. K. Asundi, Fast full-field out-of-plane deformation measurement using fringe reflectometry, Optics and Lasers in Engineering 50 (4) (2012) 529 – 533.

[38] A. Simonini, R. Theunissen, A. Masullo, M. R. Vetrano, Piv adaptive interrogation and sampling with image projection applied to water sloshing, Experimental Thermal and Fluid Science (2019) 559–574.

[39] J. Park, S. Im, H. J. Sung, J. S. Park, Piv measurements of flow around an arbitrarily moving free surface, Experiments in Fluids 56 (3) (2015).

[40] T.-H. Wang, M.-C. Lu, C.-C. Hsu, C.-C. Chen, J.-D. Tan, Liquid-level measurement using a single digital camera, Measurement 42 (4) (2009) 604 – 610. doi:https://doi.org/10.1016/j.measurement.2008.10.006.
URL http://www.sciencedirect.com/science/article/pii/S0263224108001711

[41] Y. Miao, S. Wang, Small amplitude liquid surface sloshing process detected by optical method, Optics Communications 315 (2014) 91 – 96.

[42] A. Romero-Calvo, I. R. A. J. García-Salcedo, F. Garrone, E. C.-H. G. Cano-Gómez, F. Maggi, Free surface reconstruction of opaque liquids in microgravity. Part 1: Design and on-ground testing, Acta Astronautica (2020).

[43] H. Schaub, J. L. Junkins, Analytical Mechanics of Space Systems, 4th Edition, American Institute of Aeronautics and Astronautics (AIAA), 2018.

[44] C. Rigoni, M. Pierno, G. Mistura, D. Talbot, R. Massart, J.-C. Bacri, A. Abou-Hassan, Static magnetowetting of ferrofluid drops, Langmuir 32 (30) (2016) 7639–7646.

[45] P. Souza, S. Lira, I. de Oliveira, Wetting dynamics of ferrofluids on substrates with different hydrophilicity behaviors, Journal of Magnetism and Magnetic Materials 483 (2019) 129 – 135.

[46] S. Guba, B. Horváth, I. Szalai, Examination of contact angles of magnetic fluid droplets on different surfaces in uniform magnetic field, Journal of Magnetism and Magnetic Materials 498 (2020) 166181.

[47] G. C. K. Yeh, Free and forced oscillations of a liquid in an axisymmetric tank at low-gravity environments, Journal of Applied Mechanics 34 (1) (1967) 23–28.